Chinese Chemical Letters 37 (2026) 111116

Contents lists available at ScienceDirect

Chinese Chemical Letters

journal homepage: www.elsevier.com/locate/cclet

Bi-$Bi_2Ti_2O_7$ ohmic junction: Dual electron channels driving efficient photocatalytic nitrogen fixation

Pengkun Li[a], Runjie Wu[a], Shuai Gao[c], Zeping Qin[a], Mingming Sun[a], Changzheng Wang[b,*], Wenming Sun[a], Qiang Wang[a,*]

[a] Laboratory for Micro-sized Functional Materials & College of Elementary Education and Department of Chemistry, Capital Normal University, Beijing 100048, China
[b] Beijing Key Laboratory of Functional Materials for Building Structure and Environment Remediation, Beijing University of Civil Engineering and Architecture, Beijing 100044, China
[c] College of Environmental Sciences and Engineering, The Key Laboratory of Water and Sediment Sciences (MOE), Peking University, Beijing 100871, China

ARTICLE INFO

Article history:
Received 6 December 2024
Revised 28 January 2025
Accepted 18 March 2025
Available online 19 March 2025

Keywords:
Photocatalytic
N_2 fixation
Ohmic junction
Dual electron channels
$Bi_2Ti_2O_7$

ABSTRACT

Photocatalysis uses solar energy to convert nitrogen and water directly into ammonia, helping reduce dependence on fossil fuels and offering a way to integrate the nitrogen cycle into a clean energy network. Ohmic junctions between metals and semiconductors have demonstrated significant advantages in enhancing stability and reducing carrier recombination, but their application in photocatalytic nitrogen fixation is limited due to the difficulty of work function matching and the complexity of fabrication processes. In this study, density functional theory (DFT) calculations were used to confirm the work function matching between Bi and $Bi_2Ti_2O_7$ (BTO), ensuring the formation of an Ohmic junction. A Bi-$Bi_2Ti_2O_7$ (B-BTO) composite was successfully synthesized *via* a one-step hydrothermal method, using bismuth nitrate and titanium sulfate as precursors. Compared to pure BTO, the B-BTO heterojunction, driven by dual electron injection from both metal Bi and BTO, significantly increased the ammonia synthesis rate to 686.95 μmol g^{-1} h^{-1}, making it the most active nitrogen fixation material among similar pyrochlore-based catalysts to date. The differential charge density calculations, photocurrent (*i-t*) measurements, and photoluminescence (PL) tests further validate the role of Ohmic contacts in enhancing charge transfer and prolonging carrier lifetimes. This research provides valuable insight into the application of Ohmic junctions in photocatalytic nitrogen fixation and contributes to advancements in this field.

© 2025 Published by Elsevier B.V. on behalf of Chinese Chemical Society and Institute of Materia Medica, Chinese Academy of Medical Sciences.

In the context of the global transition to low-carbon and renewable energy, photocatalytic ammonia synthesis technology provides a new pathway for ammonia production and opens up possibilities for future energy networks [1–3]. Compared to the traditional Haber-Bosch process, which requires high temperatures, high pressures, and results in high carbon emissions, photocatalysis directly converts nitrogen and water into ammonia using solar energy, demonstrating the potential to integrate the nitrogen cycle into a clean energy network [4–6].

However, current photocatalytic technologies still face challenges such as low efficiency and poor catalyst stability [7–9]. Various strategies have been proposed to design photocatalyst structures and enhance their performance, including doping [10–12], defect engineering [13,14], and heterojunctions [15–18]. Among these, Ohmic contact in metal-semiconductor heterojunctions has gained particular attention due to its low resistance and high stability [19,20]. By aligning the Fermi levels, Ohmic contact can achieve lower contact resistance, thereby reducing energy loss and electron transport resistance, which enhances reaction efficiency and response speed [21]. Additionally, the Ohmic structure helps stabilize the catalyst's performance, minimizing reductions in catalytic activity caused by photo-corrosion and chemical corrosion [22,23]. However, the complex fabrication processes for metal-semiconductor Ohmic contacts, which include precise deposition, interface modification, and post-processing, limit their widespread application. Furthermore, the conditions for forming effective Ohmic contacts require the metal's work function to be greater than that of the semiconductor, making material selection an ongoing challenge. As a result, research on enhancing photocatalytic performance using Ohmic contacts remains relatively limited [24,25].

* Corresponding authors.
E-mail addresses: changzhwang@163.com (C. Wang), qwchem@gmail.com (Q. Wang).

https://doi.org/10.1016/j.cclet.2025.111116
1001-8417/© 2025 Published by Elsevier B.V. on behalf of Chinese Chemical Society and Institute of Materia Medica, Chinese Academy of Medical Sciences.

In metal-semiconductor contacts, Bi is an ideal choice for forming an Ohmic junction. It not only effectively enhances the photocatalyst's visible light absorption but also possesses high chemical stability [15,26,27]. Moreover, Bi has a relatively low work function compared to common metals, making it more likely to form an Ohmic contact with semiconductors. $Bi_2Ti_2O_7$(BTO), as a pyrochlore structure material, shows remarkable potential in photocatalytic ammonia synthesis [5,28]. The cubic crystal structure of BTO, composed of $Bi^{3+}$and Ti^{4+} ions, provides a stable crystal framework and excellent light absorption properties. However, the rapid recombination of photogenerated electron-hole pairs limits its photocatalytic activity. By loading metallic Bi onto the surface of BTO, effective Ohmic contacts can be formed, thereby enhancing the separation and transport efficiency of photogenerated charge carriers. The favorable energy level alignment between BTO and Bi allows electrons to be effectively transferred along a low-barrier pathway, further improving photocatalytic performance.

This study developed a Bi-$Bi_2Ti_2O_7$ (B-BTO) composite material with Ohmic contact using a one-step hydrothermal method and applied it to photocatalytic nitrogen fixation for the first time. In a pure water environment under simulated sunlight, the nitrogen fixation ammonia production rate of this composite material reached 686.95 μmol g^{-1} h^{-1}, demonstrating good stability. Density functional theory (DFT) simulations determined the work functions of BTO and Bi, confirming the formation of effective Ohmic contact between the two. Furthermore, differential charge density calculations revealed that metal Bi injects electrons into the BTO substrate, enabling dual electron channels driven photocatalytic nitrogen fixation. Impedance, IT, and PL test results indicated that the composite material exhibited lower resistance, reduced electron recombination rates, and enhanced charge transfer rates. *In situ* infrared spectroscopy further confirmed the formation of NH_4^+ during the ammonia synthesis process, supporting its effectiveness in photocatalytic nitrogen fixation. This study explored the promoting effect of Ohmic contact on photocatalytic nitrogen fixation, providing new insights for future catalyst design and holding promise for achieving higher reaction efficiencies and broader applications in the field of photocatalytic ammonia synthesis.

To determine whether the n-type semiconductor BTO can form an Ohmic contact with elemental Bi ($\Phi_s \geq \Phi_m$), we first theoretically calculated the work functions of metallic Bi and BTO, which are 4.10 eV and 4.34 eV (Figs. 1a and b), respectively. This aligns with the typical conditions for forming Ohmic contacts. As shown in Fig. S1 (Supporting information), in subsequent work, we measured the work function of BTO using ultraviolet photoelectron spectroscopy (UPS), and the results confirmed that the contact between metal Bi and BTO also follows the definition of an Ohmic contact. Following this, we performed charge distribution calculations on the BTO model loaded with elemental Bi (B-BTO). Fig. 1c indicates that charge transfer primarily occurs between the loaded metallic Bi and the BTO substrate, with a significant electron depletion region formed on the Bi. This suggests that Bi can effectively inject electrons into BTO, consistent with the typical phenomenon of metal injecting electrons into a semiconductor in Ohmic contacts. This process not only enhances the availability of electrons but also provides the necessary electron source for photocatalytic reactions. Furthermore, we calculated that each Bi atom can transfer 0.18 e to the BTO substrate. This level of electron transfer enhances the electron-rich characteristics of BTO, promotes effective electron utilization, and contributes to the stability of the Ohmic contact.

In the Ohmic contact, the semiconductor substrate BTO is in an electron-rich region, and the key to photocatalytic nitrogen fixation lies in the ability of photo-generated electrons to effectively inject into the anti-bonding orbitals of N_2, thereby breaking the N≡N triple bond. Therefore, the ideal scenario is that the semiconductor BTO provides the main active sites, while the metal Bi can capture the excess photo-generated electrons during the photocatalytic nitrogen fixation process, forming an electron reservoir to prevent carrier recombination. Additionally, when the local electron concentration stored in metal Bi reaches equilibrium, electrons can flow back to BTO without barriers due to the Ohmic contact, significantly extending the effective utilization of photogenerated electrons. In the B-BTO system, the contribution of BTO to the main active sites is particularly important. To investigate this, we conducted DFT calculations on the active sites. Fig. S2 (Supporting information) shows the end-on and side-on adsorption of nitrogen molecules on the loaded Bi, with adsorption distances of 3.59 and 3.72 Å, respectively, indicating that no chemical bonds were formed. Next, we examined the adsorption of nitrogen molecules at the Bi and Ti sites in BTO. The results revealed that the adsorption distances at the proximal Bi_1 and distal Bi_2 sites were 3.64 and 3.55 Å, respectively, also showing no chemical bonding with nitrogen. Finally, the nitrogen adsorption calculation at the Ti site (Ti-N) indicated an adsorption distance of only 2.81 Å (Fig. S3 in Supporting information), which meets the bonding criteria. Moreover, during the subsequent rate-determining step ($N_2 + H^+ \rightarrow N–NH$), the Ti-N bond continued to shorten to 2.03 Å, while the N–N bond was stretched from 1.16 Å to 1.26 Å, indicating the sustained activation of nitrogen. To validate the computational results, we calculated the adsorption of nitrogen molecules at the Bi and Ti sites in BTO. We set the binding energy of the Ti site with nitrogen to 0 eV. The results indicate that the relative binding energies for nitrogen adsorption at the Bi_1 site, Bi_2 site, and the metal Bi end in the semiconductor BTO are 0.71, 0.73, and 0.93 eV, respectively. These findings are consistent with the adsorption calculations, indicating that the Ti site is the most effective nitrogen adsorption site, while the binding energies at the other Bi sites are higher than that of Ti, suggesting weaker nitrogen adsorption capabilities.

From Fig. 1d, we can see that the larger work function of BTO indicates that when metallic Bi and semiconductor BTO come into contact to form a heterojunction, electrons will spontaneously flow from the metal side to the lower energy levels of the semiconductor until the Fermi levels of both materials reach equilibrium [29]. Although the energy bands of BTO bend downward upon contact to accommodate the flow of electrons, the degree of this bending is relatively small due to the matching work functions between Bi and BTO, preventing the formation of a significant barrier. This slight band bending facilitates effective carrier transport, reducing the energy barrier at the interface, which in turn enhances electron mobility and the overall rate of the photocatalytic reaction. The barrier-free Ohmic contact characteristic not only promotes efficient electron transfer but also significantly improves the overall efficiency of the photocatalytic reaction, giving BTO a unique advantage as a photocatalyst in nitrogen fixation processes. Therefore, after the contact between metallic Bi and BTO, due to the alignment of the Fermi levels, electrons transfer from the metallic Bi to BTO, forming a low-resistance electron pathway, with electrons accumulating in the semiconductor BTO. This also supports the notion that the Ti site should be the primary active site, while the role of the Bi site is relatively limited.

In Fig. 2a, we utilized bismuth nitrate pentahydrate ($Bi(NO_3)_3·5H_2O$) and titanium sulfate ($Ti(SO_4)_2$) as the primary metal precursors to synthesize B-BTO through a one-step hydrothermal method. Polyvinylpyrrolidone (PVP) was employed as a stabilizer to prevent excessive reduction of the $Bi_2Ti_2O_7$ substrate, while an excess amount of mannitol was added to regulate the deposition of metallic Bi. The details are included in Experimental section (Supporting information). In the HRTEM image of B-BTO (Figs. 2b-f), we observed lattice fringes with spacings of 0.24 nm and 0.37 nm, corresponding to the (104) and (012)

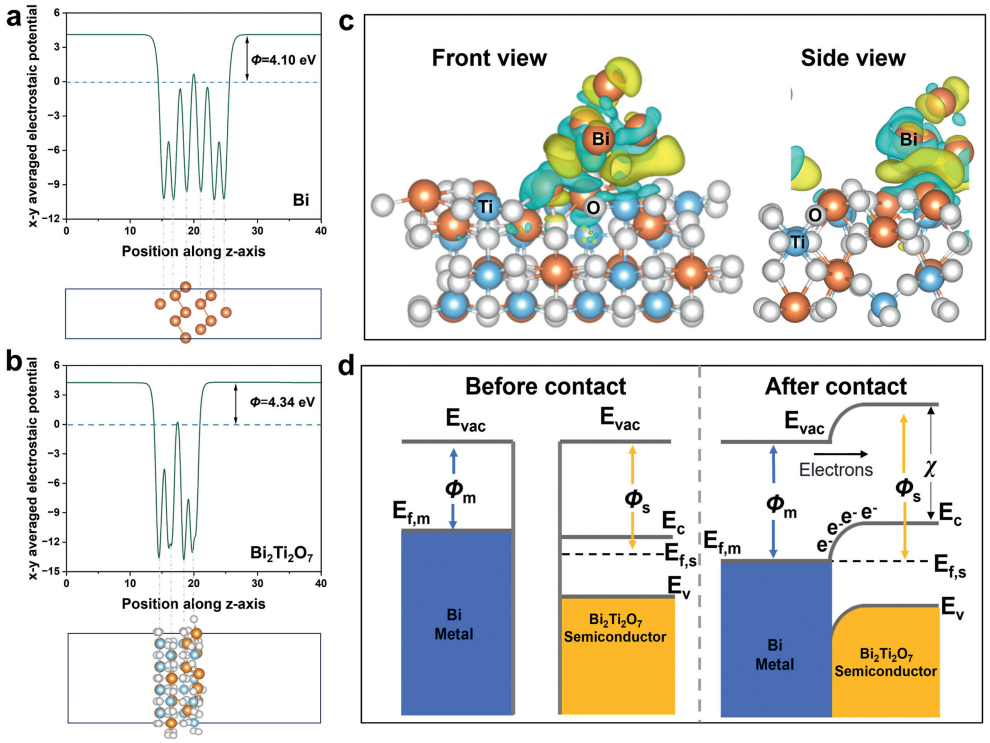


Fig. 1. The work functions of (a) Bi and (b) BT-OV. (c) Calculations of charge density difference of B-BTO. Isosurface level = 0.002 e Å^{-3}; negative charge, blue; positive charge, yellow. (d) Schematic diagram of photogenerated electron transfer before and after contact between Bi and BTO (χ, electron affinity energy; E_{vac}, vacuum level; Φ_s, work function of semiconductor; Φ_m, work function of metal).

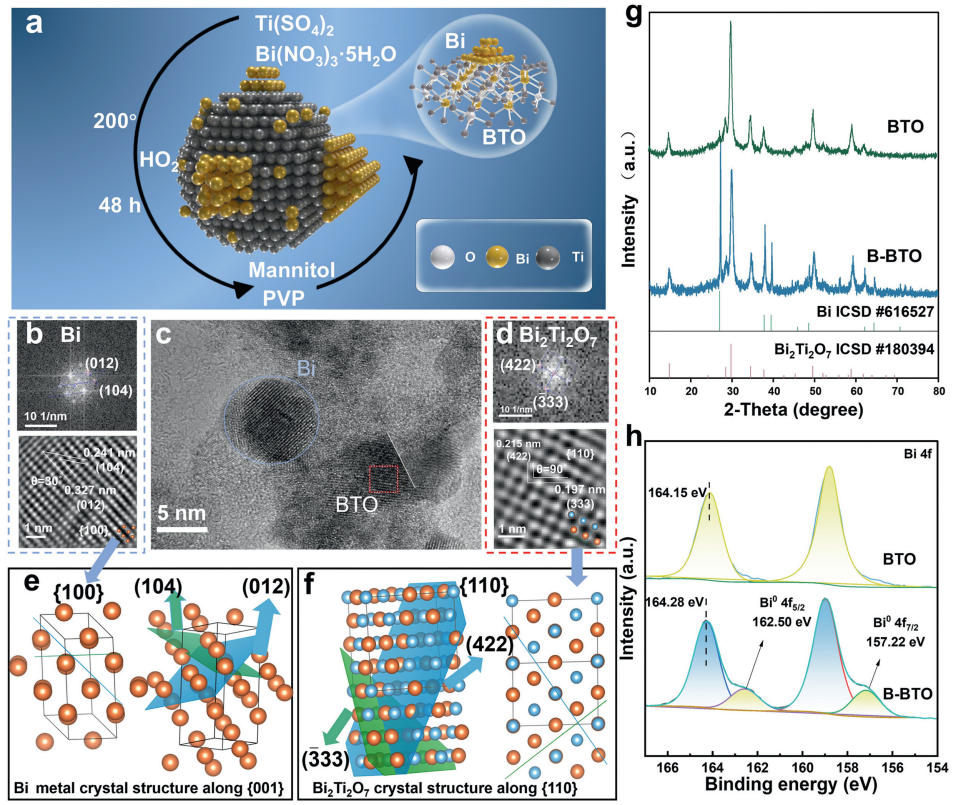


Fig. 2. (a) Schematic illustration of the preparation of B-BTO. HRTEM of B-BTO (c), and the corresponding FFT and IFFT for Bi (b) and BTO (d). Crystal structure diagrams of (e) pyrochlore BTO and (f) metal Bi. (g) XRD patterns of BTO and B-BTO. (h) High-resolution scan of the Bi 4f electrons of BTO and B-BTO.

planes of metallic Bi (Figs. 2b and e), with an interplanar angle of 30°, consistent with the crystallographic arrangement. This was further confirmed by the fast Fourier transform (FFT) and inverse Fourier transform (IFFT) patterns in Fig. 2b. The results matched the lattice parameters of ICSD #616527 ($a = b = c = 10.7225$ Å, $\alpha = \beta = \gamma = 90°$), indicating growth along the {001} direction.

Additionally, we measured lattice spacings of 0.215 nm and 0.197 nm, corresponding to the (422) and (333) planes of pyrochlore-structured $Bi_2Ti_2O_7$ (ICSD #180394), with interplanar angles matching the theoretical orthogonal relationship, showing a growth axis along {110} (Figs. 2d and f). Further measurements on pristine BTO lattice (Fig. S4 in Supporting information) revealed spacings of 0.201 nm and 0.159 nm, corresponding to the (511) and (533) planes of $Bi_2Ti_2O_7$ (ICSD #180394), with an interplanar angle of 25°, closely aligning with theoretical values, and a growth axis also along {110}, indicating consistent growth behavior between BTO and B-BTO.

To verify the successful deposition of Bi, we conducted energy-dispersive X-ray spectroscopy (EDS) analysis (Fig. S5a in Supporting information). The results revealed distinct spherical aggregation of Bi, with statistical analysis showing an average particle size of 46 nm (Fig. S5b in Supporting information), further confirming the formation of Bi particles. Moreover, scanning electron microscope (SEM) analysis (Figs. S5c and d in Supporting information) revealed that the loading of metallic Bi did not result in significant changes to the dispersion of BTO. The XRD data were analyzed using the Rietveld refinement method (Fig. S6 in Supporting information). Combined with the results of the photocatalytic ammonia synthesis gradient experiments (Fig. S7 in Supporting information), the optimal loading amount of metallic Bi was determined to be 35 wt%. The X-ray diffraction (XRD) spectrum in Fig. 2g shows diffraction peaks for BTO and B-BTO at $2\theta = 14.78°$, 28.51°, 29.80°, 34.55°, 37.76°, 49.66°, and 58.26°, corresponding to the (111), (311), (222), (400), (331), (440), and (622) planes of the pyrochlore-structured $Bi_2Ti_2O_7$ (ICSD #180394, *Fd*-3*m* space group). Notably, the XRD pattern of B-BTO exhibits a series of diffraction peaks at $2\theta = 27.17°$, 39.62°, 48.70°, and 56.01°, corresponding to the (012), (110), (202), and (024) planes of metallic Bi (ICSD #64703–5), which aligns well with the HRTEM analysis results. Subsequently, we utilized X-ray photoelectron spectroscopy (XPS) to measure the surface elemental composition and oxidation states of the samples, calibrating the data against the carbon 1s peak at a binding energy of 284.8 eV. The XPS spectra in Fig. S8 (Supporting information) show clear signals for Bi 4f, Ti 2p, and O 1s electrons at binding energies of 163.3, 485.6, and 529.9 eV, respectively. Compared to BTO, the high-resolution spectrum of Bi 4f in B-BTO exhibits double peaks at 161.98 and 156.64 eV (Fig. 2h), corresponding to Bi $4f_{5/2}$ and Bi $4f_{7/2}$, which further corroborates the successful deposition of metallic Bi [15,30].

Relative to the standard peak positions of metallic Bi^0 4f (157.01 and 162.33 eV), the Bi^0 4f peaks in B-BTO exhibit a slight blue shift (157.22 and 162.5 eV), indicating a reduction in electron cloud density and electron transfer away from Bi, which is consistent with the computational results in Fig. 1. In addition, the Ti 2p orbital in B-BTO (Fig. S9 in Supporting information) also shows a blue shift compared to that in BTO, suggesting an increase in the electron cloud density at the Ti sites. The XPS spectra in Fig. S10 (Supporting information) show three peaks at 529.25, 530.74, and 532.18 eV in BTO, corresponding to lattice oxygen, oxygen vacancies, and surface hydroxyl groups, respectively [31]. In contrast, the peaks for oxygen vacancies and surface hydroxyl groups in B-BTO exhibit a blue shift, likely due to the introduction of Bi enhancing the interactions between the oxygen atoms in the BTO lattice and their surrounding environment. Notably, the concentration of oxygen vacancies in B-BTO is significantly increased. This is further confirmed by the electron paramagnetic resonance (EPR) test results in Fig. S11 (Supporting information), where the oxygen vacancy signal ($g = 2.003$) in B-BTO is significantly stronger than that in BTO [32]. This may be due to the lattice mismatch between metallic Bi and BTO, which creates a stress field at the interface, causing oxygen atoms to escape from the BTO lattice and form oxygen vacancies. Therefore, the loading of Bi not only provides an electron buffer that reduces carrier recombination rates but also increases the concentration of oxygen vacancies.

Subsequently, we evaluated the photocatalytic ammonia generation performance of BTO and B-BTO using a 300 W xenon lamp as the light source, under conditions without cocatalysts or sacrificial agents (Fig. S12 in Supporting information). The produced NH_4^+ was detected and quantified by using the Nessler reagent colorimetric method and ion chromatography (the respective calibration curves are shown in Figs. S13 and S14, Tables S1 and S2 in Supporting information). During the detection process with Nessler's reagent, the pH range of the solution was between 7 and 10, where this method can accurately quantify the ammonia yield [33]. Additionally, before the experiment, the high-resolution XPS N 1s spectra of B-BTO were examined (Fig. S15 in Supporting information), showing no detectable signal peaks, indicating that the raw materials used in the photocatalytic reaction contained no nitrogen impurities. Fig. 3a shows the photocatalytic nitrogen fixation performance of B-BTO and BTO with high-purity nitrogen gas (99.999 %) as the feed in ultrapure water by using the Nessler reagent colorimetric method. The results indicate that B-BTO produced 1377.27 μmol/g of ammonia in 2 h at a steady rate of 686.95 μmol g^{-1} h^{-1}, while the pure BTO produced 42.71 μmol/g of ammonia in the same period at a steady rate of 24.33 μmol g^{-1} h^{-1}. Consistent results were obtained from ion chromatography measurements (Fig. S16 and Table S2 in Supporting information), where the ammonia proudction rate was estimated to be 674.07 and 23.19 μmol g^{-1} h^{-1}, respectively, confirming the reliability of the nitrogen fixation activity. From Tables S3 and S4 (Supporting information), it can be seen that the Ohmic contact structure of B-BTO has surpassed the highest performance of pyrochlore materials in photocatalytic nitrogen fixation and is also leading in recently published studies. Furthermore, no hydrogen gas was detected and only a small amount of oxygen was produced during the process (Fig. S17 in Supporting information).

From Fig. S18 (Supporting information), it can be seen that the apparent quantum efficiency (AQE) of B-BTO under monochromatic light irradiation at 365, 420, 490, and 550 nm results in ammonia yields of 1.13 %, 0.93 %, 0.79 %, and 0.58 %, respectively. To verify the accuracy of the experimental results, control experiments were conducted under different conditions. As shown in Fig. 3b, B-BTO exhibits significant nitrogen fixation activity only under visible light irradiation and a stable nitrogen supply, while no ammonia production was detected under dark conditions or in an argon atmosphere. This further confirms that the ammonia generation is achieved through photocatalytic nitrogen fixation via nitrogen gas feed.

Additionally, we tested the stability of B-BTO. After five cycles, the sample retained 98 % of its catalytic performance (Fig. 3c); the ammonia production rate showed almost no change during continuous 8 h light irradiation tests (Fig. S19 in Supporting information). XRD and high-resolution Bi 4f spectra analysis showed no significant shift in the peak positions of metallic Bi (Figs. S20 and S21 in Supporting information). These results suggest that B-BTO possesses high stability, which can be attributed to its excellent Ohmic contact characteristics. These characteristics ensure rapid charge transfer to the catalyst's active sites, reducing stress or heat accumulation caused by light irradiation and thereby preventing material degradation.

The adsorption, activation, and hydrogenation processes of nitrogen on the surface of B-BTO were further studied using *in-situ*

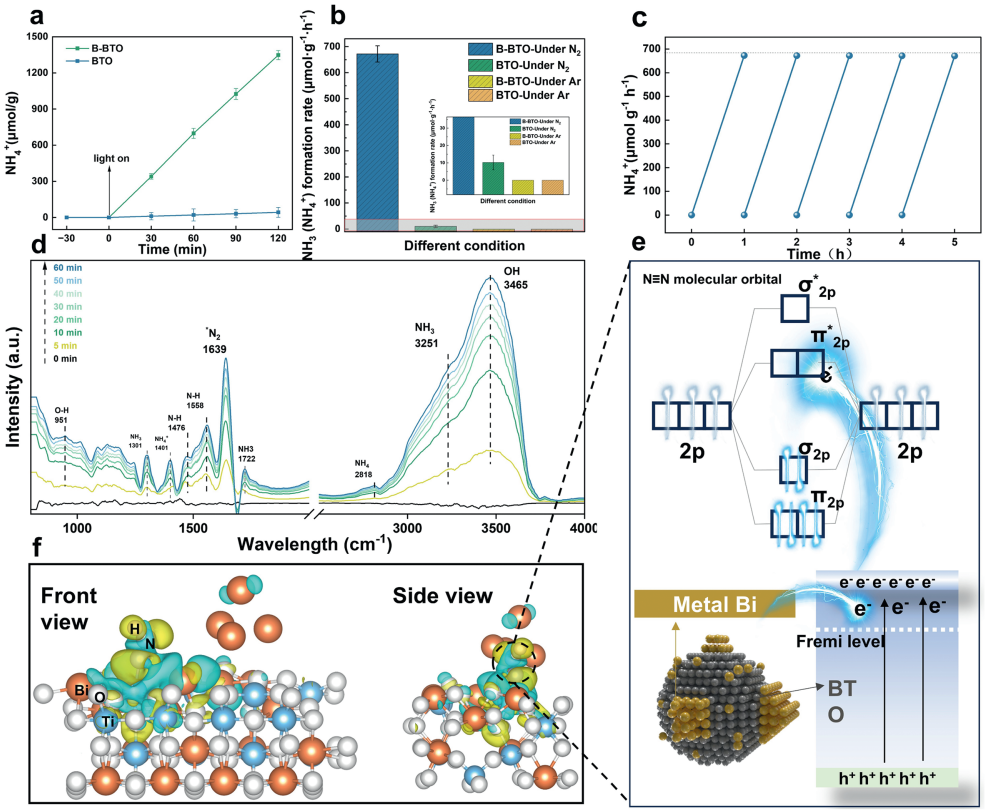


Fig. 3. (a) Quantitative determination of the generated NH_3 under visible light irradiation catalyzed by B-BTO and BTO. (b) NH_4^+ synthesis rate of B-BTO and BTO under different conditions. Inset is the zoom in of the shaded area in the figure. (c) Cycling tests of photocatalytic nitrogen fixation. (d) *In situ* FTIR spectra of B-BTO. (e) Diagram of B-BTO Activated Nitrogen. (f) Calculations of charge density difference of N–NH. Isosurface level = 0.002 e Å^{-3}; negative charge, blue; positive charge, yellow.

infrared spectroscopy. As shown in Fig. 3d, under light irradiation, the vibrational peak at 1639 cm^{-1} corresponding to chemisorbed N_2 molecules ($^*N_2$) gradually intensified [34], indicating an enhanced chemisorption capacity of B-BTO for N_2. Simultaneously, the intensities of the vibrational bands at 1301, 1722, and 3251 cm^{-1} also increased, which correspond to the characteristic vibrations of adsorbed NH_3 [35]. Peaks at 1401 and 2818 cm^{-1} are related to surface NH_4^+ [36], while the peaks at 1476 and 1558 cm^{-1} are attributed to the presence of NH intermediates [37], suggesting that light irradiation facilitates the conversion of N_2 to NH_4^+. The vibrational bands at 951 and 3465 cm^{-1} are attributed to the presence of hydroxyl groups [38]. Notably, no characteristic vibrations of N_2H_4 were detected at 1129 and 1290 cm^{-1}, further confirming the selective formation of NH_4^+ in the nitrogen fixation reaction (Fig. S22 in Supporting information).

To further investigate the mechanism of the nitrogen reduction reaction (NRR), we calculated the differential charge distribution for the rate-determining step of ammonia synthesis, specifically the protonation of N_2 to form N–NH ($N_2 + H^+ \rightarrow$ N–NH). As shown in Figs. 3e and f, there is a significant electron depletion region around the Ti sites, while an obvious electron accumulation is observed on N_2H. This occurs because the outermost d orbitals of Ti possess strong electron affinity and electron-donating capabilities. Consequently, the d orbitals of Ti hybridize with the π^* anti-bonding orbitals of nitrogen, allowing electron transfer from the Ti d orbitals to the anti-bonding orbitals of N_2. This electron transfer weakens the N≡N triple bond, effectively activating the N_2 molecule for further reaction. Notably, the electron depletion region is primarily concentrated near the surface of Bi and BTO, with the Bi metal acting as an electron reservoir, extracting electrons from BTO and temporarily storing them. This aligns with the previously discussed mechanism of Bi serving as an electronic buffer. This process effectively reduces the carrier recombination phenomenon in BTO, allowing the electrons in BTO to be transferred more efficiently to the reaction sites. The electron depletion observed between Bi and BTO, along with the electron accumulation at the Ti-N-NH sites, indicates a systematic transfer of electrons across the entire interface. Bi functions as an electron reservoir, preventing rapid recombination of electrons and holes, while the Ti sites provide critical active sites for the reduction reaction of N_2.

The UV–visible diffuse reflectance spectroscopy (UV–vis DRS) measurements (Fig. 4a) show that BTO exhibits an absorption threshold of approximately 466 nm, while the absorption range of the Bi-BTO composite material extends into the visible light region. Notably, the B-BTO composite material exhibits a weak broad peak around 550 nm, likely attributed to the surface plasmon resonance (SPR) of metallic Bi nanoparticles. Furthermore, from the corresponding Tauc plot, it can be estimated that BTO has a bandgap of 2.31 eV. Additionally, the Mott-Schottky plot (Fig. 4b) evaluates the flat band potential at multiple frequencies, revealing that the flat band potential of BTO is −0.73 eV, with a positive slope indicating that BTO behaves as an n-type semiconductor. The corresponding energy level structure is shown in Fig. S23 (Supporting information).

We conducted photoelectrochemical measurements to analyze the separation, transfer, and recombination of photogenerated charge carriers under simulated sunlight irradiation. As shown in Fig. 4c, the transient photocurrent response (TRCP) of the B-BTO composite material is significantly higher than that of BTO, indicating that the synergy between Bi and BTO enhances the generation and separation efficiency of photogenerated charge carriers. The introduction of metallic Bi improves the production of charge carriers and enhances their transport properties, ultimately result-

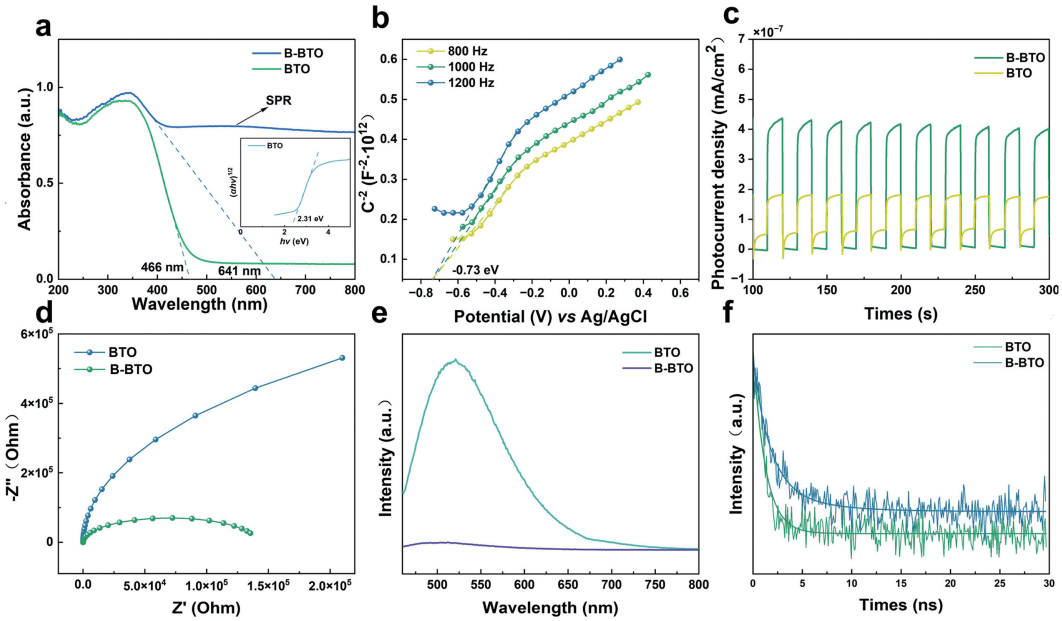


Fig. 4. (a) UV–vis absorption reflectance spectra of BTO and B-BSO. Inset is the Tauc plot of BTO. (b) Mott-Schottky plots of BTO at different frequencies in 0.5 mol/L K_2SO_4. (c) Photocurrent curves of BTO and B-BTO at various times under solar-light irradiation using a three-electrode setup. (d) Nyquist plots of BTO and B-BTO. (e) Steady-state and (f) time-resolved PL emission spectra of BTO and B-BTO. Excitation wavelength: 445 nm.

ing in a higher surface electron density. In the electrochemical impedance spectroscopy (EIS) measurements (Fig. 4d), the Nyquist plot of B-BTO shows that the charge transfer resistance (RCT) has a smaller arc radius compared to BTO, indicating that Bi-BTO exhibits a lower RCT. This further suggests that the barrier-free characteristics of Ohmic contacts significantly facilitate electron transfer, reducing interfacial resistance.

In the steady-state photoluminescence (PL) tests, we obtained results consistent with previous findings. As shown in Fig. 4e, the steady-state PL emission intensity of B-BTO is lower than that of BTO, indicating that the radiative recombination rate of photogenerated electrons and holes in the B-BTO material is significantly reduced, resulting in higher charge carrier separation efficiency and longer lifetimes. Further investigation through time-resolved transient PL (TRPL) spectroscopy measurements (Fig. 4f) confirmed this observation. In the TRPL measurements (Table S5 in Supporting innformation), we found that the decay lifetime of surface defect trap states (τ_1) is similar (1.68 ns vs. 1.25 ns), while the decay lifetime of direct transition radiation (τ_2) increased from 1.25 ns in BTO to 4.96 ns in Bi-BTO. This indicates that the primary factor affecting the lifetime of photogenerated charge carriers is not the defect states but rather the direct transition radiation of the material itself. This phenomenon can be attributed to the improved separation and migration of charge carriers at the B-BTO interface, allowing more carriers to participate in light emission or reactions. Using the formula $\tau = (A_1\tau_1^2 + A_2\tau_2^2)/(A_1\tau_1 + A_2\tau_2)$, we calculated the average PL lifetimes of BTO and B-BTO to be 1.25 ns and 2.31 ns, respectively. This result is highly consistent with the photocatalytic nitrogen fixation performance and the characteristic of Ohmic contacts in prolonging charge carrier lifetimes.

In summary, this study confirmed the work function matching between metal Bi and BTO through preliminary DFT calculations, indicating their ability to form Ohmic contacts. Subsequently, B-BTO composites were successfully synthesized using a one-step hydrothermal method. The introduction of Bi not only enhanced the material's absorption of visible light but also significantly improved the separation and transfer efficiency of photogenerated charge carriers through the formation of Ohmic contacts. At the same time, the Ohmic contact between metallic Bi and BTO has enabled B-BTO to surpass the efficiency limits of pyrochlore structures in photocatalytic nitrogen fixation. Furthermore, photoelectrochemical tests and TRPL measurements further demonstrated that B-BTO materials exhibit longer photogenerated carrier lifetimes and lower charge transfer resistance. By integrating experimental results with theoretical calculations, this study highlights the immense potential of metal-semiconductor Ohmic contacts in photocatalytic nitrogen fixation and provides new insights for developing efficient photocatalysts.

Declaration of competing interest

The authors declare that they have no known competing financial interests or personal relationships that could have appeared to influence the work reported in this paper.

CRediT authorship contribution statement

Pengkun Li: Writing – original draft, Methodology. **Runjie Wu:** Formal analysis, Data curation. **Shuai Gao:** Project administration. **Zeping Qin:** Investigation. **Mingming Sun:** Resources. **Changzheng Wang:** Supervision, Resources. **Wenming Sun:** Methodology, Formal analysis. **Qiang Wang:** Writing – review & editing, Project administration.

Acknowledgment

This work was supported by the Natural Science Foundation of China (NSFC, No. 52372212).

Supplementary materials

Supplementary material associated with this article can be found, in the online version, at doi:10.1016/j.cclet.2025.111116.

References

[1] J. Choi, B.H.R. Suryanto, D. Wang, et al., Nat. Commun. 11 (2020) 5546.
[2] W. Zhang, M. Xu, T. Wang, et al., Sep. Purif. Technol. 354 (2025) 129536.
[3] L. Wang, K. Liang, X. Yu, et al., Chin. Chem. Lett. 37 (2026) 110572.

[4] J. Zander, J. Timm, M. Weiss, et al., Adv. Energy Mater. 12 (2022) 2202403.
[5] G. Shuai, W. Runjie, S. Mingming, et al., Appl. Catal. B: Environ. 324 (2022) 122260.
[6] T. Wang, S. Qu, J. Wang, et al., J. Alloys Compd. 938 (2023) 168631.
[7] X. Chen, P. Li, S. Gao, et al., New J. Chem. 47 (2023) 13169–13176.
[8] P. Song, X. Fang, W. Jiang, et al., Trans. Tianjin Univ. 30 (2024) 211–220.
[9] S. Wu, M. Zhang, S. Huang, et al., Chin. Chem. Lett. 34 (2023) 107282.
[10] J. Zhang, W. Cui, P. Chen, et al., Catal. Today 380 (2021) 230–236.
[11] Y. Wu, H. Ji, Q. Liu, Z. Sun, et al., J. Hazard. Mater. 424 (2022) 127563.
[12] R. Cheng, C.N. Cui, Z.X. Luo, et al., Rare Met. 43 (2024) 3810–3818.
[13] X. Zu, Y. Zhao, X. Li, et al., Angew. Chem. Int. Ed. 60 (2021) 13840–13846.
[14] R. Shi, Y. Zhao, G.I.N. Waterhouse, et al., ACS Catal. 9 (2019) 9739–9750.
[15] R. Wu, S. Gao, C. Jones, et al., Adv. Funct. Mater. 34 (2024) 2314051.
[16] C. Zhao, X. Li, L. Yue, et al., ACS Appl. Nano Mater. 6 (2023) 15709–15720.
[17] H. Wang, Z. Chen, Y. Shang, et al., ACS Catal. 14 (2024) 5779–5787.
[18] X. Gong, P. Song, C. Han, et al., Energy Mater. 3 (2023) 300016.
[19] F. Rao, G. Zhu, W. Zhang, et al., Appl. Catal. B: Environ. 281 (2020) 119481.
[20] B. Dai, W. Zhao, H. Huang, et al., J. Colloid Interface Sci. 616 (2022) 163–176.
[21] Y. Fan, X. Hao, N. Yi, et al., Appl. Catal. B: Environ. 357 (2024) 124313.
[22] W.A. Qureshi, X. Hong, X. He, et al., Chemosphere 291 (2022) 132987.
[23] J. Li, J. Yao, Q. Yu, et al., Appl. Catal. B: Environ. 351 (2024) 123950.
[24] S. Yadav, M. Aslam, V. Garg, et al., Silicon 14 (2022) 10901–10908.
[25] H. Yang, Y. Li, D.P. Norton, et al., Appl. Phys. Lett. 86 (2005) 172103.
[26] J. Liu, T. Wang, Q. Nie, et al., Appl. Surf. Sci. 559 (2021) 149970.
[27] Q. Wang, X. Bai, Y. Zhang, et al., ACS Appl. Nano Mater. 3 (2020) 1934–1941.
[28] P. Li, R. Wu, P. Li, et al., Adv. Sci. 11 (2024) 2408829.
[29] K. Wei, H. Li, H. Gu, et al., Adv. Funct. Mater. 32 (2022) 2200498.
[30] Y. Zhang, J. Di, X. Qian, et al., Appl. Catal. B: Environ. 299 (2021) 120680.
[31] S. Gao, H. Ji, P. Yang, et al., Small 19 (2023) 2206114.
[32] H. Zhou, D. Zhang, H. Xie, et al., Adv. Mater. 35 (2023) 2300914.
[33] Y. Zhao, R. Shi, X. Bian, et al., Adv. Sci. 6 (2019) 1802109.
[34] G. Wang, T. Huo, Q. Deng, et al., Appl. Catal. B: Environ. 310 (2022) 121319.
[35] Y. Zhang, J. Di, X. Zhu, et al., Appl. Catal. B: Environ. 323 (2023) 122148.
[36] Y. Zhao, L. Zheng, R. Shi, et al., Adv. Energy Mater. 10 (2020) 2002199.
[37] J. Yuan, W. Feng, Y. Zhang, et al., Adv. Mater. 36 (2024) 2303845.
[38] S. Gao, R. Wu, M. Sun, et al., Appl. Catal. B: Environ. 324 (2023) 122260.